

In Situ Electron Microscopy Imaging and Quantitative Structural Modulation of Nanoparticle Superlattices

Juyeong Kim,^{†,‡} Matthew R. Jones,[§] Zihao Ou,[†] and Qian Chen^{*,†,‡,⊥}

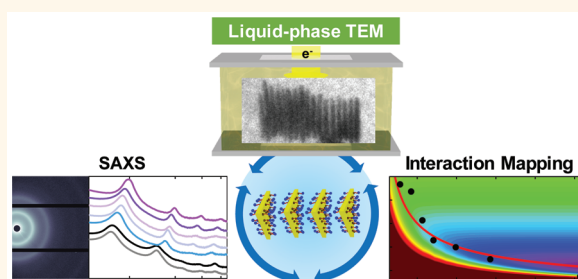
[†]Department of Materials Science and Engineering, [‡]Frederick Seitz Materials Research Laboratory, and [⊥]Department of Chemistry, University of Illinois, Urbana, Illinois 61801, United States

[§]Department of Chemistry, University of California, Berkeley, California 94720, United States

S Supporting Information

ABSTRACT: We use liquid-phase transmission electron microscopy (LP-TEM) to characterize the structure and dynamics of a solution-phase superlattice assembled from gold nanoprisms at the single particle level. The lamellar structure of the superlattice, determined by a balance of interprism interactions, is maintained and resolved under low-dose imaging conditions typically reserved for biomolecular imaging. In this dose range, we capture dynamic structural changes in the superlattice in real time, where contraction and smaller steady-state lattice constants are observed at higher electron dose rates. Quantitative analysis of the contraction mechanism based on a combination of direct LP-TEM imaging, ensemble small-angle X-ray scattering, and theoretical modeling allows us to elucidate: (1) the superlattice contraction in LP-TEM results from the screening of electrostatic repulsion due to as much as a 6-fold increase in the effective ionic strength in the solution upon electron beam illumination; and (2) the lattice constant serves as a means to understand the mechanism of the *in situ* interaction modulation and precisely calibrate electron dose rates with the effective ionic strength of the system. These results demonstrate that low-dose LP-TEM is a powerful tool for obtaining structural and kinetic properties of nanoassemblies in liquid conditions that closely resemble real experiments. We anticipate that this technique will be especially advantageous for those structures with heterogeneity or disorder that cannot be easily probed by ensemble methods and will provide important insight that will aid in the rational design of sophisticated reconfigurable nanomaterials.

KEYWORDS: nanoassemblies, reorganization kinetics, liquid-phase TEM, gold nanoprism superlattice, interaction modeling, SAXS



Self-assembly of nanoparticles into complex architectures promises access to collective photonic,^{1–3} plasmonic,^{4–6} electronic,^{7–9} catalytic,^{10,11} and magnetic¹² functionalities that are tunable and may even be adaptable in response to changes in external conditions.^{13–16} An understanding of internanoparticle interactions and structuring kinetics in liquids is essential for predictive nanoparticle assembly, which remains a challenge.^{17,18} Classical colloidal theories developed for interactions between micron-sized particles do not simply rescale at nanometer dimensions because of multiscale collective effects and the nonadditivity of nanoscale interactions.^{18–21} Ideally one would address this by analyzing directly the dynamic motion and assembly of individual nanoparticles. However, experimental studies of this sort are complicated by the need to acquire images with the appropriate time and spatial resolution while nanoparticles interact freely in liquids to form into superstructures.

Most *in situ* observations of nanoparticle assembly in solution use small-angle X-ray scattering (SAXS), which probes assembled structures in reciprocal space.^{13–15,22,23} SAXS has minimal disturbance to the native sample solution during measurement and high resolution in detecting structural order. It is limited, however, by its ensemble nature, which offers little insight into the real-time motions and interactions of single nanoparticles and complicates interpretation of structural heterogeneity/disorder.

On the other hand, liquid-phase transmission electron microscopy (LP-TEM) readily achieves single-nanoparticle imaging in liquids^{24–32} and allows experimental interpretation of nanoparticle interactions and assembly dynamics.^{33–38} For example, LP-TEM has been used to observe nanoparticle

Received: August 4, 2016

Accepted: October 10, 2016

monolayer formation during solvent drying³³ and the assembly of gold spheres,^{34–36} gold rods,³⁷ and CdSe/CdS octapods³⁸ into linear chains. Based on a statistical analysis of single nanoparticle motion trajectories, our earlier work reported a quantitative map of nanoparticle interactions inside LP-TEM.³⁷ The limitation of LP-TEM is the effect of the imaging electron beam, which has been shown to greatly alter the liquid components through radiolysis reactions.^{27–29} For instance, the radiolysis of water,³⁹ the widely used solvent for metallic nanoparticle and biomolecule-directed assemblies, generates ionic and reactive species (OH^- , H^+ , hydrated e^- , OH , *etc.*) as a function of electron beam dose rates (number of electrons imposed onto the sample per unit area per unit time). These reactions frequently perturb the solution considerably, convoluting the interpretation of the data and making the results challenging to be used to guide nanoparticle assembly in standard experimental conditions outside TEM. It is thus critical to experimentally quantify how local changes in the liquid environment within the illuminated area consequently influence nanoparticle interactions and assembly dynamics.

Here we use low-dose LP-TEM to characterize one-dimensional (1D) nanoprism superlattices. We resolve the real-space structure of a hydrated crystalline nanoparticle superlattice and its structural change in response to local changes in the liquid. The quantitative correlation among LP-TEM images, theoretical modeling, and ensemble measurements of lattice constants by SAXS enables us to understand the mechanism of electron beam-mediated nanoparticle interactions and to reproduce identical structural reorganization of the assembly outside TEM. We observe that the dose rates typically used in cryogenic EM imaging of biomolecules ($1\text{--}10 \text{ e}^-/(\text{\AA}^2\cdot\text{s})$),⁴⁰ which are lower than the dose rates commonly used in earlier LP-TEM studies (Figure S1 and Table S1), are required to prevent the superlattices from collapsing completely. Within the optimized dose rate range ($1\text{--}6 \text{ e}^-/(\text{\AA}^2\cdot\text{s})$), the contraction of the lattice constant, *i.e.*, the center-to-center d spacing between prisms (Figure 1A), is quantitatively modulated by electron beam dose rates. We see the “*in situ*” and “outside TEM” correlation we establish here as a critical step to generalize single-nanoparticle insights on nanoparticle assembly learned from LP-TEM, at a spatiotemporal resolution not accessible by other means, to direct predictable assembly in real experimental conditions.

RESULTS AND DISCUSSION

The superlattices used in this work are defined by evenly spaced gold triangular nanoprisms aligned face-to-face, heretofore referred to as meta-rods (Figure 1A). While the meta-rods represent a rich and important class of nanoparticle superlattices, with collective properties that are sensitive to the spatial arrangement of component nanoparticles,^{1,4,5,7–9,11,12} they have previously been characterized at the ensemble level.⁴¹ The meta-rods are prepared by functionalizing gold prisms ($89.3 \pm 9.1 \text{ nm}$ in edge length and $7.5 \pm 0.3 \text{ nm}$ in thickness) with a dense monolayer of alkyl-thiol ligands, rationally designed to induce robust solution-phase assembly behavior (see Materials and Methods in the Supporting Information, Figure S2). Specifically, carboxyl-terminated thiols are exchanged with the native cetyltrimethylammonium bromide (CTAB) ligands on the prism surface.^{42–44} The strong gold–thiol bond allows for the system to be prepared in such a way so as to have a low concentration of free ligands. This minimizes the contribution of depletion forces⁴¹ and facilitates

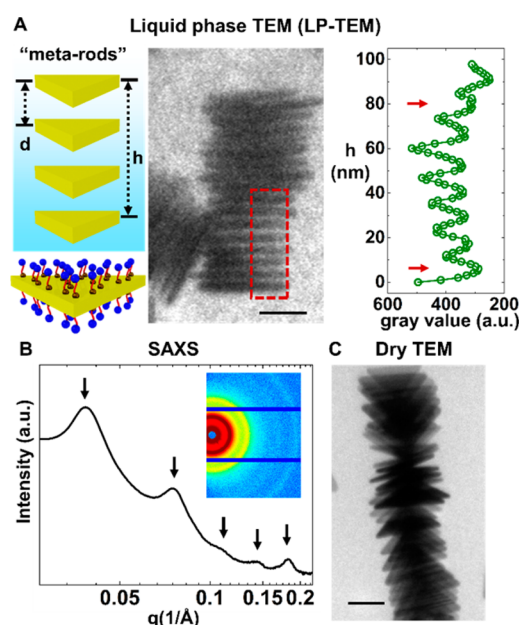


Figure 1. Characterizations of meta-rods. (A) A schematic (left, not drawn to the scale) of meta-rods in 0.15 M pH = 8 PBS buffer solution labeling the d spacing and the meta-rod length h , a LP-TEM image showing a meta-rod lying flat on the SiN_x liquid window (middle), and the intensity profile of the TEM image region boxed by red dotted lines showing the intensity averaged horizontally as a function of the vertical axis due to alternating prisms (dark in TEM) and interstices (bright in TEM), from which we measure the d spacing in LP-TEM (right). The red arrows highlight positions corresponding to the starting and ending prisms shown in the red box of the TEM image. (B) SAXS spectrum of the meta-rods in 0.15 M pH = 8 PBS buffer solution. The black arrows highlight the peak positions in the spectrum, from which we measure the d spacing in SAXS. The inset shows the 2D scattering image of the same meta-rod solution. (C) A TEM image of dried meta-rods as a comparison, where capillary forces have collapsed the 3D arrangement of meta-rods. Scale bars: 50 nm.

theoretical modeling of interprism interactions for mechanistic understanding. An aqueous pH = 8 phosphate buffer solution (PBS) is used as the liquid medium to ensure complete deprotonation of the ligands into negatively charged $-\text{COO}^-$ groups ($\text{pK}_a = 3.5\text{--}3.7$, Figure S3A), which excludes interparticle hydrogen-bonding effects ($-\text{COOH}\cdots\text{OHOC}-$).⁴³ The high buffer concentration (0.15 M) maintains a constant pH and keeps the surface charge density of prisms constant even with potential radiolysis-generated H^+ or OH^- species (see the evaluation of beam-induced pH effects in Figure S3B). Under these conditions, prisms assemble face-to-face through a balance of electrostatic repulsion and van der Waals attraction.

Figure 1A shows a typical LP-TEM image of 1D meta-rods lying flat on the SiN_x window composing the liquid cell sample chamber, showing visible interstices between nearest-neighbor prisms which indicate preservation of the solvent/ligand layers between the particles. The LP-TEM image was taken at a dose rate of $10 \text{ e}^-/(\text{\AA}^2\cdot\text{s})$ and an accelerating voltage of 200 kV. The real-space TEM image allows us to measure the d spacing directly from the intensity profile across parallel neighboring prisms (Figure 1A); the d spacing is consistent between different pairs of neighboring prisms ($12.2 \pm 1.0 \text{ nm}$). Movie S1 shows that at the stable state the intensity profile fluctuates and still generates a consistent d spacing over time. Such direct

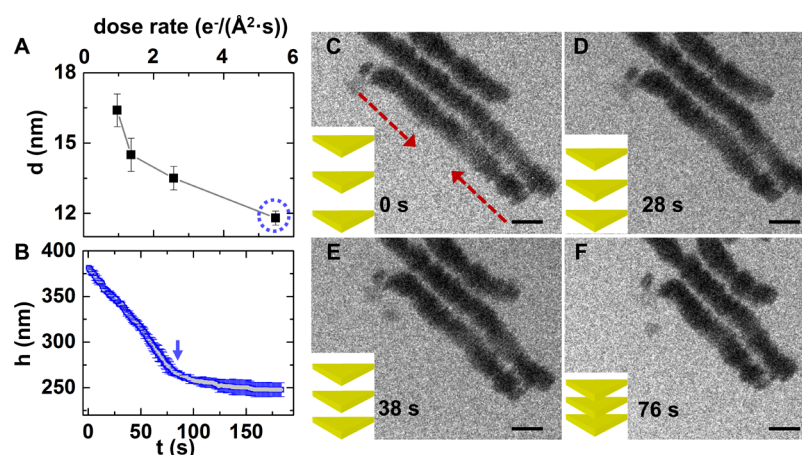


Figure 2. Meta-rod contraction in LP-TEM. (A) The d spacing–dose rate curve showing the electron beam effect on the stable meta-rod d spacing in LP-TEM. The dotted circle is the condition where detailed analysis and meta-rod contraction dynamics are shown in (B–F). (B) The master $h(t)$ – t curve averaged from the $h(t)$ – t curves of five different meta-rods (Figure S4) after normalization by the number of prisms inside one meta-rod, N . The blue arrow shows the equilibrium state of meta-rods. (C–F) Time-lapsed LP-TEM images of meta-rods, demonstrating a shrinking of their total length over time. The dotted arrows indicate the direction of the meta-rod contraction. Scale bar: 100 nm.

measurement of nanoparticle spatial organization in liquids may be generalized to other complicated multicomponent superlattices that exhibit heterogeneity and localized disorders, the structural elucidation of which using SAXS could be challenging.^{13–15,22,23} For the purpose of comparison, Figure 1C is a typical TEM image of a dried superlattice dropcast on a TEM grid. Evaporation-induced capillary forces disturb the periodic features of the meta-rods and warp the structure so that it may flatten on the substrate.

Comparison between the averaged d spacings of the same meta-rod solution measured in LP-TEM and with SAXS shows that the electron beam modulates nanoparticle interactions. In Figure 1B, both the 2D scattering image and the plot of scattered intensity $I(q)$ versus scattering vector q clearly feature sharp diffraction peaks at integer spacings, consistent with a highly ordered 1D lamellar structure.⁴¹ We obtain a d spacing of 16.4 ± 0.7 nm from the q value of the first-order peak in the SAXS spectrum, larger than what is measured from LP-TEM (12.2 ± 1.0 nm). In other words, meta-rods contract in LP-TEM and stabilize at a shifted steady-state d spacing determined by the re-established liquid environment under beam irradiation.

The meta-rod contraction can be qualitatively explained by the screening of electrostatic repulsion due to the generation of ionic species during radiolysis. Quantitative understanding of the influence of the beam on nanoparticle interactions has been limited due to the difficulty of measuring the ion concentration change inside LP-TEM.^{34,37,39} The ions produced from radiolysis are transient and localized, present only in the beam illumination area, which is challenging to quantify using ensemble electrochemical measurements or elemental analysis methods within a TEM. Theoretical calculations based on radiolysis reaction networks predict the steady-state concentrations of many species when the solvent is pure water, but this does not extend readily to highly salted liquids due to their poorly understood radiolysis kinetics.³⁹ In contrast, here the d spacing of meta-rods serves as a convenient measurable parameter for quantification of beam modulated nanoparticle interactions.

The degree of meta-rod contraction is controlled by electron beam dose rates in LP-TEM. We take care to minimize electron beam exposure to a region with meta-rods of interest prior to imaging (see Materials and Methods in the Supporting Information). Within the dose rate range of 1 – 6 $e^-/(\text{\AA}^2\cdot\text{s})$, the d spacing of meta-rods measured in LP-TEM decreases monotonically with increasing dose rates (Figure 2A), and we are able to capture the contraction dynamics of meta-rods from their native states. For example, at a dose rate of 5.5 $e^-/(\text{\AA}^2\cdot\text{s})$, time-lapsed TEM images that are collected immediately after beam irradiation show that the meta-rods contract until they reach a plateau value of stable length (Figure 2B–F, Movie S2). The d spacing is measured by $d = h/N$ (Table S2), where h is the meta-rod length and N is the time-invariant number of prisms comprising one meta-rod given that the time scales of prism assembly and prism exchange between meta-rods are both slower than the imaging experiment. The $h(t)$ – t plot in Figure 2B reveals two important features of the contraction dynamics. First, it takes ~ 1 min to reach the steady-state, longer than the estimated time needed for radiolysis reactions to complete (ms to seconds).³⁹ Because prisms comprising the meta-rods need to move collectively to achieve their new equilibrium positions, it is important to use the stable d spacing, not a random spacing at time t , as the indicator of the re-established liquid environment. Second, the $h(t)$ – t curves of five different meta-rods (Figure S4) converge to one master curve after being normalized by N (Figure 2B). The final d spacing is independent of N , which is consistent with the hypothesis that the meta-rods respond sensitively to local changes in liquids and demonstrates their robustness as an *in situ* indicator of liquid-mediated nanoparticle interactions.

In the above dose range, most previous LP-TEM work using nanoparticle-based chemical reactions as probes of radiation effects detected no changes (see our literature survey in Figure S1 and Table S1). Meta-rods are more sensitive and respond to as low as 1 $e^-/(\text{\AA}^2\cdot\text{s})$ (Figure S5 and Table S2) due to their ability to detect ion concentrations directly (see below), while reaction probes (e.g., nanoparticle nucleation and etching events) are only responsive when the cumulative change in the

redox environment in irradiated liquids is sufficient to overcome reaction barriers.^{45,46}

The monotonic decrease in the stable d spacing with increasing dose rates is understood through theoretical modeling on nanoparticle interaction energetics and validated by SAXS of meta-rods. The modeling accounts for the pairwise interparticle interactions for prisms aligned face-to-face, specifically the competition between van der Waals attraction (E_{vdW}) and electrostatic repulsion (E_{el} , resulting from the charged ligands on the prism surface). We assume constant surface charge density on the prisms in the model for two reasons: the ligands do not dissociate in the low dose rate range and stay fully deprotonated in the pH = 8 PBS buffer solution. Under these conditions, both interactions have analytical expressions (see Theory and Calculations in the Supporting Information),^{41,47} and the stable d spacing is derived from the face-to-face configuration of prisms at the minimum total interaction energy (E_{total}), as shown in Figure 3A. The prism size does not change the stable d spacing position, but only the magnitude of the interaction energy minimum.

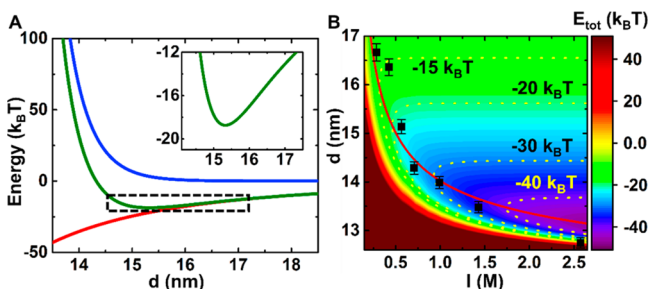


Figure 3. Theoretical calculations of interprism pairwise interactions in meta-rods with face-to-face particle alignment. (A) The interaction energy– d spacing curve for gold nanoprisms at 0.15 M pH = 8 PBS (red curve: van der Waals attraction energy (E_{vdW}), blue curve: electrostatic repulsion energy (E_{el}), and green curve: total interaction energy ($E_{total} = E_{el} + E_{vdW}$)). The inset shows a magnified view of the boxed energy well for E_{total} to show the energy minimum position. (B) The 2D interaction energy landscape showing how the pairwise interaction changes with different ionic strengths and d spacing. Black squares: d spacing for different ionic strengths obtained from SAXS measurements, red solid line: the calculated lowest interaction energy and stable d spacing at different ionic strengths, and yellow dotted lines: equal energy contours.

According to the model, the interprism interactions and the stable d spacing are dependent on material and liquid properties that rely solely on two parameters that change under beam irradiation: the temperature of the liquid, that determines thermal fluctuation and the values of physical properties, and the ionic strength of the liquid, that quantifies the electrostatic screening effect from solvated ions. Figure S6 shows the total interaction energy as a function of liquid temperature while keeping ionic strength constant (0.15 M PBS buffer). The temperature range (25 to 60 °C) far exceeds the predicted change in temperature caused by high energy electron flux in LP-TEM experiments (a few Kelvins).^{48,49} Nevertheless, over the range of (overestimated) temperatures, the meta-rods are predicted to exhibit a negligible change in the d spacing albeit with more shallow energy minimums as the temperature increases. Next, the total interaction energy map as a function of ionic strength at a fixed pH = 8 shows that the

calculated equilibrium d spacing steadily decreases as ionic strength increases (Figure 3B, red line). This confirms that the interactions directing the meta-rod assembly respond selectively to the local ionic strength. The calculated free-energy minimums are in the range of -10 to $-50 k_B T$, strong enough to hold the prisms against thermal fluctuation (Figure S7A).

Following these predictions, we control the temperature and ionic strength in the meta-rod solutions, respectively, and measure the stable d spacing using SAXS (Figure 4). The stable

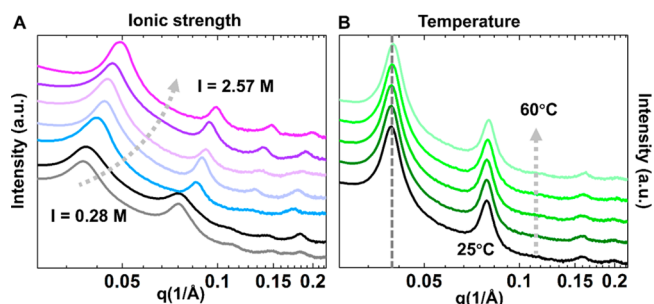


Figure 4. SAXS measurements of meta-rods at different ionic strengths and temperatures. (A) SAXS spectra of meta-rods at different ionic strengths outside the TEM. From bottom to top: 0.28, 0.42, 0.57, 0.71, 0.99, 1.43, and 2.57 M. (B) SAXS spectra of meta-rods in PBS (0.15 M, pH = 8) measured at different temperatures. From bottom to top: 25, 30, 40, 50, and 60 °C.

d spacing as a function of ionic strength measured from the SAXS spectra of meta-rods (Figure 4A and Table S3) is overlaid as squares in the energy diagram of Figure 3B and matches well with the predicted stable d spacing at the lowest energy configurations (solid red line in Figure 3B). The insensitivity of the d spacing to temperature change is also validated by SAXS measurements of meta-rods at elevated temperatures (Figure 4B). This agreement is consistent with the underlying mechanistic picture that the electron beam irradiation induces ionic strength increases that cause the meta-rods to contract.

It is important to note that under the conditions of high salt concentration (ionic strength >1 M) and closely spaced charged surfaces of the prisms (<5 nm), dipole–dipole, dipole–charge, and charge–charge correlations are no longer negligible,^{50,51} but work together to pose great challenges for conventional theories on electrostatics. In the above interaction calculations, we take into account the modification of the dielectric constant of water due to the high salt content in order to achieve a good agreement with the experimental data (Figure S7B).^{50,51} Nonetheless, the measured d spacing at the highest salt concentration is lower than the calculated value as shown in Figure 3B, likely due to the strong charge–charge correlations that effectively “screen” the electrostatic repulsion more than what is predicted by the linearized Poisson–Boltzmann equation.⁵² Precise correlation between the theory and experiment is challenging due to the lack of vigorously tested theories, since most colloidal and nanoparticle systems aggregate randomly at these salt concentrations.⁵³ The unique geometry of large, flat, and charged prism surfaces keeps the meta-rods stable and thus renders them excellent candidate structures to probe electrostatics under extreme conditions.

The one-to-one relation of d spacing *versus* dose rate and d spacing *versus* ionic strength allows us to correlate dose rate in LP-TEM and ionic strength outside with a high level of

accuracy. As shown in regime 1 of Figure 5, even at dose rates that previous LP-TEM studies have shown to induce minimal

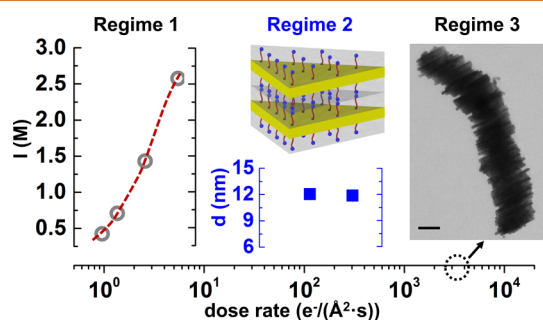


Figure 5. Electron beam effect on interprism interactions and assemblies over a wide range of dose rates. Left: Changes to the ionic strength in regime 1 of dose rates with an initial solution of 0.15 M PBS (pH = 8). The dotted line is a guide to the eye. Middle: The d spacing of meta-rods stays constant in dose rate regime 2, where ligand layers on the adjacent nanoprisms (highlighted in gray) are in physical contact. Right: The TEM image in regime 3 shows that at high dose rates nanoprisms fuse into a large solid structure. Scale bar: 50 nm.

nanoparticle reactions ($5.5 \text{ e}^-/(\text{\AA}^2\cdot\text{s})$), the ionic strength increases up to 6 times (from 0.4 to 2.6 M) and causes a significant modulation of the electrostatic environment. This degree of increase is qualitatively consistent with predictions generated by solving radiolysis reactions of pure water (Figure S8A). As a reference, the working range of ionic strength and pH at different dose rates for unbuffered solution is estimated in Figure S8B, which can be used as a method to quantitatively modulate the liquid conditions *in situ*. The exact degree of radiation-induced ionic strength increase depends on the native liquid components and initial ionic strength, which can be quantified using our meta-rod design (from as low as 0.2 M to as high as 2.6 M ionic strength, Figure S9).

Going beyond the low dose rate range, we investigate two additional regimes of distinct irradiation effects on nanoparticle assemblies. In regime 2 ($\sim 6\text{--}300 \text{ e}^-/(\text{\AA}^2\cdot\text{s})$) shown in Figure 5, the stable d spacing values stay constant around 12.3 nm regardless of dose rates. We hypothesize that the meta-rods have contracted to a physical limit where the ligand layers of adjacent prisms are in physical contact. Steric hindrance of the ligand layers prevents the meta-rods from contracting further despite strong beam irradiation. This trend indicates that the ligand monolayers are stable in this dose range and have a thickness of ~ 2.4 nm, consistent with reported literature values.^{43,54–56} Note that at this distance, even our corrected electrostatic repulsion calculation does not apply due to ultrasmall (<0.2 nm) separation between charged ligand layers from neighboring particles. Calculation of the Debye length, the characteristic range of electrostatic repulsion, over a range of ionic strengths (Figure S10), confirms that electrostatic interactions decay to a value smaller than single atoms at an ionic strength larger than that in regime 1. In addition, the observation of a constant ligand thickness confirms that in the low-dose regime (Regime 1), the ligands are not dissociated under the electron beam. Regime 3 in Figure 5 represents the conventional dose rates used in dry TEM imaging of inorganic materials and most LP-TEM studies.^{46,57,58} In this range, the stable d spacing decreases below the minimum value observed in regime 2. For example, at $3400 \text{ e}^-/(\text{\AA}^2\cdot\text{s})$, the meta-rods

contract drastically, adjacent prisms experience physical contact, and the particles fuse into a single rod-shaped mass of gold as shown in the inset TEM image of Figure 5 and Movie S3. This fusion indicates a change in the nature of the radiation effect; presumably the electron beam can deposit enough energy to agitate the ligand–nanoparticle bonds, removing the ligands and destabilizing the surface of the nanoparticles in a manner that allows atomic contact between gold atoms.^{59–61} For regime 3, the detailed mechanism is not within the scope of this work, but the dramatic structural changes detected by the meta-rods serve as a cautionary note for future LP-TEM work.

CONCLUSIONS

Our work shows the *in situ* imaging and modulation of assembled nanoparticle superlattices using LP-TEM, which is further calibrated and reproduced in practical experimental conditions through a combination of SAXS and theoretical modeling. Going beyond the ability to quantify the dynamic pathways and fundamental interactions governing nanoparticle assemblies, these data suggest practical guidelines for LP-TEM studies in general, as the degree of beam-induced change in the ionic strength is sufficient to reconfigure large-scale nanoparticle assemblies. The ability to quantify radiation-induced liquid changes is potentially influential for two prominent directions of future LP-TEM studies: imaging soft materials (e.g., polymers, DNA, proteins) and electrochemical processes (e.g., catalysis, corrosion, lithiation in batteries).^{27–29} For soft materials, besides intermolecular interactions, their stable conformation and function depend intimately on the intricate interplay of electrostatic and van der Waals forces. For example, previous LP-TEM studies that demonstrated complementary DNA base-pairing induced by the electron beam might now be explained by electrostatic screening between neighboring phosphate groups as a secondary effect of beam irradiation.³⁶ For electrochemical processes, the generation of redox-active species concurrent with ionic strength changes is expected to modify the thermodynamics and kinetics of any observed reactions. We expect in both cases that our quantitative calibration of dose rate can serve as a general guideline for (1) good operating dose rates and (2) interpreting and even correcting for radiation effects, for example, by eliminating additional electrostatic screening.

METHODS AND EXPERIMENTAL DETAILS

Synthesis of Gold Triangular Nanoprisms. Gold triangular nanoprisms were synthesized according to literature methods.^{62,63} First, gold nanoparticle seeds were prepared by sequential addition of aqueous solutions of HAuCl_4 (250 μL , 10 mM), sodium citrate (500 μL , 10 mM), and NaBH_4 (300 μL , 10 mM) into 18.95 mL of water. The seed solution was aged at 40–45 $^\circ\text{C}$ for 15 min and then cooled down to room temperature. Triangular nanoprisms were grown by mixing aqueous solutions of HAuCl_4 (250 μL , 10 mM), NaOH (50 μL , 100 mM), ascorbic acid (50 μL , 100 mM), and gold seed solution (22 μL) in an aqueous solution of CTAB (9 mL, 50 mM) containing 50 μM of NaI. After 30 min, an aqueous solution of NaCl (0.9 mL, 2 M) was added to the purple solution for purification. After 2 h, the solution was centrifuged to separate spherical particles and dispersed in 50 mM CTAB.

Ligand Exchange and Meta-Rod Assembly. The prism solution (9 mL) in 50 mM CTAB was centrifuged and redispersed in water. A thiol solution in water (HS-

(CH₂)₁₁(OC₂H₄)₆OCH₂COOH) (44.6 μL, 7.93 mM) was added to the prism solution. After 30 min of incubation, 0.15 M PBS (pH = 8) was added to the prism solution. Black sediments were observed after ~15 h of incubation, which indicates the formation of meta-rods.

SAXS Measurement. Black sediments of meta-rods in liquid were gently transferred to a quartz capillary tube. The SAXS spectrum was measured using a home-built setup (Forvis Technologies, Santa Barbara) composed of a Xenocs GeniX3D CuKα ultralow divergence X-ray source (1.54 Å/ 8 keV) with a divergence of ~1.3 mrad and a Pilatus 300 K 20 Hz hybrid pixel detector (Dectris). Ionic strength variation was achieved through changing the PBS (pH = 8) concentration.

LP-TEM Imaging. A Protochips Poseidon 210 liquid flow holder was used for LP-TEM imaging under a JEOL 2100 Cryo TEM with a LaB₆ emitter at 200 kV. A Gatan Ultrascan charge-coupled device camera with a 0.1 s exposure time per frame at a rate of 1.3 fps was used for recording TEM movies. An aliquot of the meta-rods in PBS (0.15 M, pH = 8) was loaded on an oxygen plasma-cleaned SiN_x microchip (window: 550 μm × 20 μm, 150 nm spacer flow echip, Protochips) and assembled with the top SiN_x microchip (window: 550 μm × 20 μm) into the liquid holder. Electron dose rate control was achieved by varying spot size and beam intensity.

Theory and Calculations. The model considers the competition between van der Waals attraction (E_{vdW}) that favors smaller d spacing and electrostatic repulsion (E_{el}) that prefers larger d spacing. The equilibrium d spacing is where the net pairwise interaction energy ($E_{\text{total}} = E_{\text{el}} + E_{\text{vdW}}$) between nearest-neighboring prisms aligned face-to-face reaches a stable minimum. We consider only pairwise interactions because the decay lengths of both interactions (~15 to 20 nm) are smaller than the smallest possible distance between next nearest prisms. At high ionic strength (>1.0 M), ion–dipole correlation is taken into account for the electrostatic contribution to the total interaction energy.

ASSOCIATED CONTENT

Supporting Information

The Supporting Information is available free of charge on the ACS Publications website at DOI: 10.1021/acsnano.6b05270.

Materials and methods, theory and calculations, Figures S1–S10, and Tables S1–S5 (PDF)

A synchronized movie including a LP-TEM movie (left) of meta-rods in PBS pH = 8 (0.15 M) solution stabilized at a dose rate of 10 e⁻/(Å²·s) and the intensity profile (right, same notations as in Figure 1A) showing the alternating prisms and interstices, which does not change as a function of time after stabilized. The real time is shown in the time stamp. The movie is played at 8 fps, 6× real time. Scale bar: 50 nm (AVI)

A LP-TEM movie showing the contraction of meta-rods in PBS pH = 8 (0.15 M) from native states at a dose rate of 5.5 e⁻/(Å²·s). Contraction of meta-rods gradually occurs over 80 s. The movie is played at 10 fps, 8× real time. Scale bar: 300 nm (AVI)

A synchronized movie including a LP-TEM movie (left) showing meta-rods in PBS (0.15 M) at a dose rate of 3400 e⁻/(Å²·s) and how the total length of the meta-rod (L_1+L_2) at the bottom of the movie changes with time. The real time is shown in the time stamp. The movie is played at 8 fps, 6× real time. The high-intensity beam

gives rise to a rapid contraction upon illumination before the movie acquisition. Gold nanoprisms are fused together over time. Scale bar: 50 nm (AVI)

AUTHOR INFORMATION

Corresponding Author

*E-mail: qchen20@illinois.edu.

Notes

The authors declare no competing financial interest.

ACKNOWLEDGMENTS

We thank Matthew Kulzick, a senior scientist at BP and Prof. Jian-Min Zuo at the University of Illinois for helpful discussions on the manuscript. This work was supported by the U.S. Department of Energy, Office of Basic Energy Sciences, Division of Materials Sciences and Engineering under award no. DE-FG02–07ER46471, through the Frederick Seitz Materials Research Laboratory at the University of Illinois. M.R.J. acknowledges the Arnold and Mabel Beckman Foundation for a postdoctoral fellowship.

REFERENCES

- (1) Poyser, C. L.; Czerniuk, T.; Akimov, A.; Diroll, B. T.; Gauld, E. A.; Salasyuk, A. S.; Kent, A. J.; Yakovlev, D. R.; Bayer, M.; Murray, C. B. Coherent Acoustic Phonons in Colloidal Semiconductor Nanocrystal Superlattices. *ACS Nano* **2016**, *10*, 1163–1169.
- (2) Saran, R.; Curry, R. Lead Sulphide Nanocrystal Photodetector Technologies. *Nat. Photonics* **2016**, *10*, 81–92.
- (3) Konstantatos, G.; Sargent, E. H. Nanostructured Materials for Photon Detection. *Nat. Nanotechnol.* **2010**, *5*, 391–400.
- (4) Tao, A.; Sinsermsuksakul, P.; Yang, P. Tunable Plasmonic Lattices of Silver Nanocrystals. *Nat. Nanotechnol.* **2007**, *2*, 435–440.
- (5) Young, K. L.; Ross, M. B.; Blaber, M. G.; Rycenga, M.; Jones, M. R.; Zhang, C.; Senesi, A. J.; Lee, B.; Schatz, G. C.; Mirkin, C. A. Using DNA to Design Plasmonic Metamaterials with Tunable Optical Properties. *Adv. Mater.* **2014**, *26*, 653–659.
- (6) Fan, J. A.; Wu, C.; Bao, K.; Bao, J.; Bardhan, R.; Halas, N. J.; Manoharan, V. N.; Nordlander, P.; Shvets, G.; Capasso, F. Self-Assembled Plasmonic Nanoparticle Clusters. *Science* **2010**, *328*, 1135–1138.
- (7) Talapin, D. V.; Lee, J.-S.; Kovalenko, M. V.; Shevchenko, E. V. Prospects of Colloidal Nanocrystals for Electronic and Optoelectronic Applications. *Chem. Rev.* **2010**, *110*, 389–458.
- (8) Dong, A.; Jiao, Y.; Milliron, D. J. Electronically Coupled Nanocrystal Superlattice Films by *In Situ* Ligand Exchange at the Liquid–Air Interface. *ACS Nano* **2013**, *7*, 10978–10984.
- (9) Kagan, C. R.; Murray, C. B. Charge Transport in Strongly Coupled Quantum Dot Solids. *Nat. Nanotechnol.* **2015**, *10*, 1013–1026.
- (10) Yamada, Y.; Tsung, C.-K.; Huang, W.; Huo, Z.; Habas, S. E.; Soejima, T.; Aliaga, C. E.; Somorjai, G. A.; Yang, P. Nanocrystal Bilayer for Tandem Catalysis. *Nat. Chem.* **2011**, *3*, 372–376.
- (11) Kang, Y.; Ye, X.; Chen, J.; Qi, L.; Diaz, R. E.; Doan-Nguyen, V.; Xing, G.; Kagan, C. R.; Li, J.; Gorte, R. J.; Stach, E. A.; Murray, C. B. Engineering Catalytic Contacts and Thermal Stability: Gold/Iron Oxide Binary Nanocrystal Superlattices for CO Oxidation. *J. Am. Chem. Soc.* **2013**, *135*, 1499–1505.
- (12) Cheon, J.; Park, J.-I.; Choi, J.-S.; Jun, Y.-W.; Kim, S.; Kim, M. G.; Kim, Y.-M.; Kim, Y. J. Magnetic Superlattices and Their Nanoscale Phase Transition Effects. *Proc. Natl. Acad. Sci. U. S. A.* **2006**, *103*, 3023–3027.
- (13) Zhang, Y.; Pal, S.; Srinivasan, B.; Vo, T.; Kumar, S.; Gang, O. Selective Transformations between Nanoparticle Superlattices via the Reprogramming of DNA-Mediated Interactions. *Nat. Mater.* **2015**, *14*, 840–847.

- (14) Zhao, Y.; Thorkelsson, K.; Mastroianni, A. J.; Schilling, T.; Luther, J. M.; Rancatore, B. J.; Matsunaga, K.; Jinnai, H.; Wu, Y.; Poulsen, D.; Frechet, J. M. J.; Paul Alivisatos, A.; Xu, T. Small-Molecule-Directed Nanoparticle Assembly towards Stimuli-Responsive Nanocomposites. *Nat. Mater.* **2009**, *8*, 979–985.
- (15) Kim, Y.; Macfarlane, R. J.; Jones, M. R.; Mirkin, C. A. Transmutable Nanoparticles with Reconfigurable Surface Ligands. *Science* **2016**, *351*, 579–582.
- (16) Gerling, T.; Wagenbauer, K. F.; Neuner, A. M.; Dietz, H. Dynamic DNA Devices and Assemblies Formed by Shape-Complementary, Non-Base Pairing 3D Components. *Science* **2015**, *347*, 1446–1452.
- (17) Grzelczak, M.; Vermant, J.; Furst, E. M.; Liz-Marzán, L. M. Directed Self-Assembly of Nanoparticles. *ACS Nano* **2010**, *4*, 3591–3605.
- (18) Bishop, K. J. M.; Wilmer, C. E.; Soh, S.; Grzybowski, B. A. Nanoscale Forces and Their Uses in Self-Assembly. *Small* **2009**, *5*, 1600–1630.
- (19) Silvera Batista, C. A.; Larson, R. G.; Kotov, N. A. Nonadditivity of Nanoparticle Interactions. *Science* **2015**, *350*, 1242477.
- (20) Min, Y.; Akbulut, M.; Kristiansen, K.; Golan, Y.; Israelachvili, J. The Role of Interparticle and External Forces in Nanoparticle Assembly. *Nat. Mater.* **2008**, *7*, 527–538.
- (21) French, R. H.; Parsegian, V. A.; Podgornik, R.; Rajter, R. F.; Jagota, A.; Luo, J.; Asthagiri, D.; Chaudhury, M. K.; Chiang, Y.-M.; Granick, S.; Kalinin, S.; Kardar, M.; Kjellander, R.; Langreth, D. C.; Lewis, J.; Lustig, S.; Wesolowski, D.; Wettlaufer, J. S.; Ching, W.-Y.; Finnis, M.; et al. Long Range Interactions in Nanoscale Science. *Rev. Mod. Phys.* **2010**, *82*, 1887–1944.
- (22) Lu, F.; Yager, K. G.; Zhang, Y.; Xin, H.; Gang, O. Superlattices Assembled through Shape-Induced Directional Binding. *Nat. Commun.* **2015**, *6*, 6912.
- (23) Li, T.; Senesi, A. J.; Lee, B. Small Angle X-Ray Scattering for Nanoparticle Research. *Chem. Rev.* **2016**, *116*, 11128.
- (24) Park, J.; Elmlund, H.; Ercius, P.; Yuk, J. M.; Limmer, D. T.; Chen, Q.; Kim, K.; Han, S. H.; Weitz, D. A.; Zettl, A.; Alivisatos, A. P. 3D Structure of Individual Nanocrystals in Solution by Electron Microscopy. *Science* **2015**, *349*, 290–295.
- (25) Smeets, P. J. M.; Cho, K. R.; Kempen, R. G. E.; Sommerdijk, N. A. J. M.; De Yoreo, J. J. Calcium Carbonate Nucleation Driven by Ion Binding in a Biomimetic Matrix Revealed by *In Situ* Electron Microscopy. *Nat. Mater.* **2015**, *14*, 394–399.
- (26) Chen, Q.; Smith, J. M.; Park, J.; Kim, K.; Ho, D.; Rasool, H. I.; Zettl, A.; Alivisatos, A. P. 3D Motion of DNA-Au Nanoconjugates in Graphene Liquid Cell Electron Microscopy. *Nano Lett.* **2013**, *13*, 4556–4561.
- (27) Ramachandramoorthy, R.; Bernal, R.; Espinosa, H. D. Pushing the Envelope of *In Situ* Transmission Electron Microscopy. *ACS Nano* **2015**, *9*, 4675–4685.
- (28) De Yoreo, J. J.; Sommerdijk, N. A. J. M. Investigating Materials Formation with Liquid-Phase and Cryogenic TEM. *Nat. Rev. Mater.* **2016**, *1*, 16035.
- (29) Ross, F. M. Opportunities and Challenges in Liquid Cell Electron Microscopy. *Science* **2015**, *350*, aaa9886.
- (30) Liao, H.-G.; Zherebetsky, D.; Xin, H.; Czarnik, C.; Ercius, P.; Elmlund, H.; Pan, M.; Wang, L.-W.; Zheng, H. Facet Development During Platinum Nanocube Growth. *Science* **2014**, *345*, 916–919.
- (31) Peckys, D. B.; Baudoin, J.-P.; Eder, M.; Werner, U.; de Jonge, N. Epidermal Growth Factor Receptor Subunit Locations Determined in Hydrated Cells with Environmental Scanning Electron Microscopy. *Sci. Rep.* **2013**, *3*, 2626.
- (32) Welch, D. A.; Woehl, T. J.; Park, C.; Faller, R.; Evans, J. E.; Browning, N. D. Understanding the Role of Solvation Forces on the Preferential Attachment of Nanoparticles in Liquid. *ACS Nano* **2016**, *10*, 181–187.
- (33) Park, J.; Zheng, H.; Lee, W. C.; Geissler, P. L.; Rabani, E.; Alivisatos, A. P. Direct Observation of Nanoparticle Superlattice Formation on by Using Liquid Cell Transmission Electron Microscopy. *ACS Nano* **2012**, *6*, 2078–2085.
- (34) Liu, Y.; Lin, X.-M.; Sun, Y.; Rajh, T. *In Situ* Visualization of Self-Assembly of Charged Gold Nanoparticles. *J. Am. Chem. Soc.* **2013**, *135*, 3764–3767.
- (35) Grogan, J. M.; Rotkina, L.; Bau, H. H. *In Situ* Liquid-Cell Electron Microscopy of Colloid Aggregation and Growth Dynamics. *Phys. Rev. E* **2011**, *83*, 061405.
- (36) Keskin, S.; Besztejan, S.; Kassier, G.; Manz, S.; Bücker, R.; Riekeberg, S.; Trieu, H. K.; Rentmeister, A.; Miller, R. J. D. Visualization of Multimerization and Self-Assembly of DNA-Functionalized Gold Nanoparticles Using In-Liquid Transmission Electron Microscopy. *J. Phys. Chem. Lett.* **2015**, *6*, 4487–4492.
- (37) Chen, Q.; Cho, H.; Manthiram, K.; Yoshida, M.; Ye, X.; Alivisatos, A. P. Interaction Potentials of Anisotropic Nanocrystals from the Trajectory Sampling of Particle Motion Using *In Situ* Liquid Phase Transmission Electron Microscopy. *ACS Cent. Sci.* **2015**, *1*, 33–39.
- (38) Sutter, E.; Sutter, P.; Tkachenko, A. V.; Krahn, R.; de Graaf, J.; Arciniegas, M.; Manna, L. *In Situ* Microscopy of the Self-Assembly of Branched Nanocrystals in Solution. *Nat. Commun.* **2016**, *7*, 11213.
- (39) Grogan, J. M.; Schneider, N. M.; Ross, F. M.; Bau, H. H. Bubble and Pattern Formation in Liquid Induced by an Electron Beam. *Nano Lett.* **2014**, *14*, 359–364.
- (40) Henderson, R. The Potential and Limitations of Neutrons, Electrons and X-Rays for Atomic Resolution Microscopy of Unstained Biological Molecules. *Q. Rev. Biophys.* **1995**, *28*, 171–193.
- (41) Young, K. L.; Jones, M. R.; Zhang, J.; Macfarlane, R. J.; Esquivel-Sirvent, R.; Nap, R. J.; Wu, J.; Schatz, G. C.; Lee, B.; Mirkin, C. A. Assembly of Reconfigurable One-Dimensional Colloidal Superlattices due to a Synergy of Fundamental Nanoscale Forces. *Proc. Natl. Acad. Sci. U. S. A.* **2012**, *109*, 2240–2245.
- (42) Millstone, J. E.; Park, S.; Shuford, K. L.; Qin, L.; Schatz, G. C.; Mirkin, C. A. Observation of a Quadrupole Plasmon Mode for a Colloidal Solution of Gold Nanoprisms. *J. Am. Chem. Soc.* **2005**, *127*, 5312–5313.
- (43) Jones, M. R.; Macfarlane, R. J.; Prigodich, A. E.; Patel, P. C.; Mirkin, C. A. Nanoparticle Shape Anisotropy Dictates the Collective Behavior of Surface-Bound Ligands. *J. Am. Chem. Soc.* **2011**, *133*, 18865–18869.
- (44) Leary, R. K.; Kumar, A.; Straney, P. J.; Collins, S. M.; Yazdi, S.; Dunin-Borkowski, R. E.; Midgley, P. A.; Millstone, J. E.; Ringe, E. Structural and Optical Properties of Discrete Dendritic Pt Nanoparticles on Colloidal Au Nanoprisms. *J. Phys. Chem. C* **2016**, *120*, 20843–20851.
- (45) Sutter, E. A.; Sutter, P. W. Determination of Redox Reaction Rates and Orders by *In Situ* Liquid Cell Electron Microscopy of Pd and Au Solution Growth. *J. Am. Chem. Soc.* **2014**, *136*, 16865–16870.
- (46) Wu, J.; Gao, W.; Wen, J.; Miller, D. J.; Lu, P.; Zuo, J.-M.; Yang, H. Growth of Au on Pt Icosahedral Nanoparticles Revealed by Low-Dose *In Situ* TEM. *Nano Lett.* **2015**, *15*, 2711–2715.
- (47) Walker, D. A.; Browne, K. P.; Kowalczyk, B.; Grzybowski, B. A. Self-Assembly of Nanotriangle Superlattices Facilitated by Repulsive Electrostatic Interactions. *Angew. Chem., Int. Ed.* **2010**, *49*, 6760–6763.
- (48) Zheng, H.; Claridge, S. A.; Minor, A. M.; Alivisatos, A. P.; Dahmen, U. Nanocrystal Diffusion in a Liquid Thin Film Observed by *In Situ* Transmission Electron Microscopy. *Nano Lett.* **2009**, *9*, 2460–2465.
- (49) White, E. R.; Mecklenburg, M.; Shevitski, B.; Singer, S. B.; Regan, B. C. Charged Nanoparticle Dynamics in Water Induced by Scanning Transmission Electron Microscopy. *Langmuir* **2012**, *28*, 3695–3698.
- (50) Levy, A.; Andelman, D.; Orland, H. Dielectric Constant of Ionic Solutions: A Field-Theory Approach. *Phys. Rev. Lett.* **2012**, *108*, 227801.
- (51) Levy, A.; Andelman, D.; Orland, H. Dipolar Poisson-Boltzmann Approach to Ionic Solutions: A Mean Field and Loop Expansion Analysis. *J. Chem. Phys.* **2013**, *139*, 164909.
- (52) Guldbbrand, L.; Jönsson, B.; Wennerström, H.; Linse, P. Electrical Double Layer Forces. A Monte Carlo Study. *J. Chem. Phys.* **1984**, *80*, 2221–2228.

(53) Meakin, P. Formation of Fractal Clusters and Networks by Irreversible Diffusion-Limited Aggregation. *Phys. Rev. Lett.* **1983**, *51*, 1119–1122.

(54) Pale-Grosdemange, C.; Simon, E. S.; Prime, K. L.; Whitesides, G. M. Formation of Self-Assembled Monolayers by Chemisorption of Derivatives of Oligo(ethylene glycol) of Structure HS-(CH₂)₁₁(OCH₂CH₂)_mOH on Gold. *J. Am. Chem. Soc.* **1991**, *113*, 12–20.

(55) Harder, P.; Grunze, M.; Dahint, R.; Whitesides, G. M.; Laibinis, P. E. Molecular Conformation in Oligo(ethylene glycol)-Terminated Self-Assembled Monolayers on Gold and Silver Surfaces Determines Their Ability to Resist Protein Adsorption. *J. Phys. Chem. B* **1998**, *102*, 426–436.

(56) Lee, J. K.; Kim, Y.-G.; Chi, Y. S.; Yun, W. S.; Choi, I. S. Grafting Nitrotriacyclic Groups onto Carboxylic Acid-Terminated Self-Assembled Monolayers on Gold Surfaces for Immobilization of Histidine-Tagged Proteins. *J. Phys. Chem. B* **2004**, *108*, 7665–7673.

(57) Zheng, H.; Smith, R. K.; Jun, Y.-W.; Kisielowski, C.; Dahmen, U.; Alivisatos, A. P. Observation of Single Colloidal Platinum Nanocrystal Growth Trajectories. *Science* **2009**, *324*, 1309–1312.

(58) Lu, J.; Aabdin, Z.; Anand, U.; Mirsaidov, U. Effect of Electron Beam on Nanoparticle Dynamics in Solution During *In Situ* TEM Observation. *Microsc. Microanal.* **2015**, *21*, 257–258.

(59) Egerton, R. F. Control of Radiation Damage in the TEM. *Ultramicroscopy* **2013**, *127*, 100–108.

(60) Zan, R.; Ramasse, Q. M.; Jalil, R.; Georgiou, T.; Bangert, U.; Novoselov, K. S. Control of Radiation Damage in MoS₂ by Graphene Encapsulation. *ACS Nano* **2013**, *7*, 10167–10174.

(61) Niu, K.-Y.; Liao, H.-G.; Zheng, H. Visualization of the Coalescence of Bismuth Nanoparticles. *Microsc. Microanal.* **2014**, *20*, 416–424.

(62) Jones, M. R.; Mirkin, C. A. Bypassing the Limitations of Classical Chemical Purification with DNA-Programmable Nanoparticle Recrystallization. *Angew. Chem., Int. Ed.* **2013**, *52*, 2886–2891.

(63) O'Brien, M. N.; Jones, M. R.; Kohlstedt, K. L.; Schatz, G. C.; Mirkin, C. A. Uniform Circular Disks with Synthetically Tailorable Diameters: Two-Dimensional Nanoparticles for Plasmonics. *Nano Lett.* **2015**, *15*, 1012–1017.